Wiley Analytical Science

The Current State of Reconstruction Technologies for 3D X-ray Microscopy including Algorithmic Innovation for AI-based Recovery

April 26, 10:00am - 11:00am EDT

Many properties can only be fully understood in 3D, such as porosity and tortuosity in porous materials, network connection maps in neuroscience, or mechanical properties in 3D additively manufactured structures. X-ray microscopy provides a unique method to image samples non-destructively in 3D across a wide range of materials and life sciences.

Watch this session during the WAS Virtual Conference:

Nicolas Guenichault, Ph.D.

Dr. Stephen T. Kelly, Ph.D.

Register Now

This talk is sponsored by ZEISS

ADVANCED OPTICAL MATERIALS
www.advopticalmat.de

Experimental Observation of Vector Bound States in the Continuum

*Huizhen Zhang, Weixuan Zhang, Shaohu Chen, Pengfei Duan, Junjie Li, Lei Shi,**
*Jian Zi, and Xiangdong Zhang**

Bound states in the continuum (BICs) provide an important way for creating photonic devices reliant upon optical modes with high Q-factors. However, current experimental implementations of BICs in photonic crystal (PhC) slabs only possess a certain polarization, which fundamentally restricts their use to surface-enhanced applications assisted by scalar-polarized near fields. In this work, vector BICs in PhC slabs are theoretically designed and experimentally realized. In theory, the symmetry-protected vector BICs can be constructed by tuning geometric parameters of the PhC slab, where the coalescence of eigenfrequencies for a pair of TE- and TM-like modes appears. It is found that the homogeneous superchiral fields with three orders of magnitude larger than circular polarized lights can be achieved, assisted by vector quasi-BICs. Furthermore, Si_3N_4 PhC slabs are experimentally fabricated and their band structures are measured. It is shown that a pair of symmetry-protected BICs with TE- and TM-like polarizations can coalesce with each other at a suitable value for the diameter of array holes, indicating the realization of vector BICs. This work can possess important applications in the field of ultrasensitive detections of molecular chirality.

1. Introduction

Bound states in the continuum (BICs) are localized resonant states in open systems that cannot couple with radiating channels. It was first proposed by Neumann and Wigner in 1929 within an electronic system,[1] and has attracted much interest in the past decade. Although it is originally proposed in quantum mechanical systems, the physical origin of BICs is derived from the wave interference effect. Therefore, the concept of BIC has been extended to many classical wave systems, and extensive experimental verifications of BICs have been realized.[2–13] It is noted that photonic structures possessing BICs usually contain resonant modes with ultrahigh Q-factors, making those exotic states have important applications.[14–19] To date, most of previous investigations are focused on photonic BICs with a certain polarization. Some recent theoretical studies have shown the existence of vector BICs,[20,21] which exhibit the full-vector polarization with respect to a pair of orthogonal modes. The proposed vector BICs can play key roles in the surface-enhanced detection technologies assisted with vector near fields.

On the other hand, chirality refers to the property that an object cannot be superimposed onto its mirror image.[22] It exists in most biomolecules as well as chemically synthesized drugs. The molecular activity is often determined by their handedness.[23,24] Thus, the high-efficient discrimination of chiral enantiomers is critically important.[25,26] Superchiral field, which possesses a larger optical chirality

---

H. Zhang, W. Zhang, X. Zhang
Key Laboratory of Advanced Optoelectronic Quantum Architecture and Measurements of Ministry of Education
Beijing Key Laboratory of Nanophotonics and Ultrafine Optoelectronic Systems
School of Physics
Beijing Institute of Technology
Beijing 100081, P. R. China
E-mail: zhangxd@bit.edu.cn

S. Chen, L. Shi, J. Zi
State Key Laboratory of Surface Physics
Key Laboratory of Micro- and Nano-Photonic Structures (Ministry of Education) and Department of Physics
Fudan University
Shanghai 200433, P. R. China
E-mail: lshi@fudan.edu.cn

P. Duan
CAS Center for Excellence in Nanoscience
CAS Key Laboratory of Nanosystem and Hierarchical Fabrication
National Center for Nanoscience and Technology (NCNST)
Beijing 100190, P. R. China

J. Li
Beijing National Laboratory for Condensed Matter Physics
Institute of Physics
Chinese Academy of Sciences
Beijing 100190, P. R. China

The ORCID identification number(s) for the author(s) of this article can be found under https://doi.org/10.1002/adom.202203118.

DOI: 10.1002/adom.202203118

than circular polarized light (CPL), can significantly enhance the molecular chiroptical effect, allowing for the ultrasensitive detection of chiral molecules. In this case, the investigation of superchiral fields has bloomed in the last ten years, and intense theoretical and experimental studies have been devoted to the generation of superchiral near fields with the help of artificial nanostructures.[27–31] While, most previous nanostructures are suffering from many problems, such as high optical losses,[32–41] extrinsic CD caused by the nanostructure itself [40] and coexistence of chiral near fields with different handedness.[32–41] To solve those problems, suitably engineered low-loss achiral nanostructures, which exhibit high Q-factors and the simultaneously excitation of two orthogonal polarization modes, are required. In this case, the vector BICs with high Q-factors and dual-polarization mode profiles, can be regarded as an ideal candidate to fulfill the surface-enhanced chiral detection. However, up to date, all of previous works on the vector BICs are focusing in theory, and no experimental demonstration on the existence of vector BICs has been carried out.

In this work, we provide the first experimental observation of vector BICs in PhC slabs. We show that the symmetry-protected vector BIC can be constructed by suitably tuning geometric parameters of the PhC slab, where the formation of vector BIC is confirmed by the coalesce of eigenfrequencies of a pair of transverse-electric (TE)- and transverse-magnetic (TM)-like BICs at the center of momentum space. Moreover, we find that the homogeneous superchiral fields with three orders of magnitude larger than CPLs can be achieved by suitably exciting the vector quasi-BICs. Such a strong enhancement is the largest one in current state-of-the-art designs. Furthermore, we experimentally fabricate Si_3N_4 PhC slabs with different sizes of cylinder holes, where the associated band structures are measured. We find that the vector BIC with a dual polarization appears with a suitable size of hole diameters. Our work suggests a useful way to realize ultrasensitive detections of molecular chirality.

2. The Theoretical Design of Vector BICs in Photonic Crystal Slabs

We start to consider a Si_3N_4 PhC slab with a square array of cylindrical holes coated on the silica substrate, as shown in **Figure 1**a. The period and thickness of PhC slab are labeled by a and h, and the diameter of holes is marked by d. The refractive indexes of background medium, PhC slab, and substrate

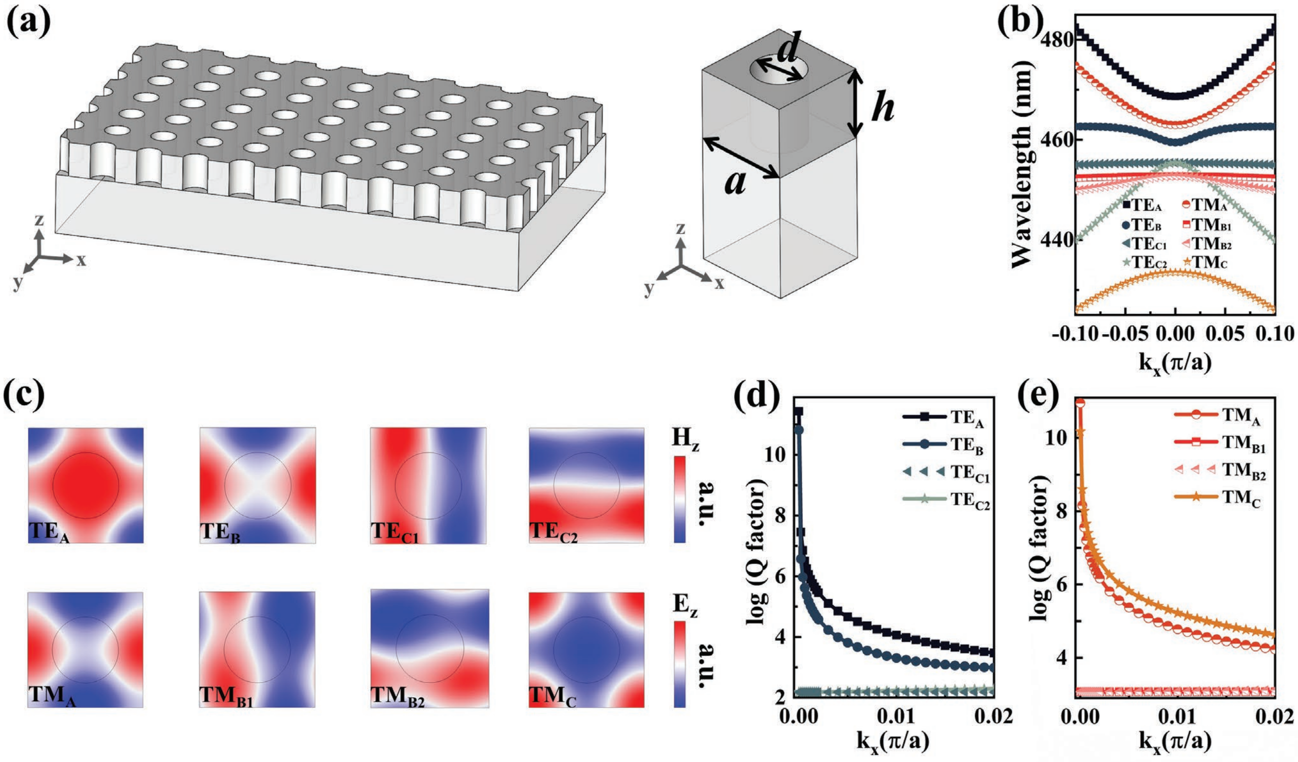

Figure 1. a) The Diagram of the symmetric photonics crystal slab. The parameters are chosen as a = 270 nm, t = 154 nm, n_p = 2.02, and n_s = 1.47, respectively. b) Band structure of the photonic crystal slab with a = 270 nm, t = 154 nm, d = 155 nm. The different resonance modes are labelled as TE_A/TE_B/ TE_{C1}/ TE_{C2}, and TM_A/TM_{B1}/TM_{B2}/TM_C. respectively. TE_A, TE_B, TE_{C1}, and TE_{C2} modes are represented by black squares, dark green circles, green triangles, and light green stars, while TM_A, TM_{B1}, TM_{B2}, and TM_C modes are represented by half-filled wine circles, red squares, pink triangles, and orange stars. c) Eigenstates of all these resonance states at Γ point. d) Q-factors of TE-like modes. Black squares, dark green circles, and light green stars represent Q-factors of TE_A, TE_B, and TE_{C2} modes, respectively. Green triangles represent the Q-factor of TE_{C1} mode. e) Q-factors of TM-like modes. Half-filled wine circles, red squares, and orange stars represent Q-factors of TM_A, TM_{B1}, and TM_C modes, respectively. Half-filled pink triangles represent the Q-factor of TM_{B2} mode.

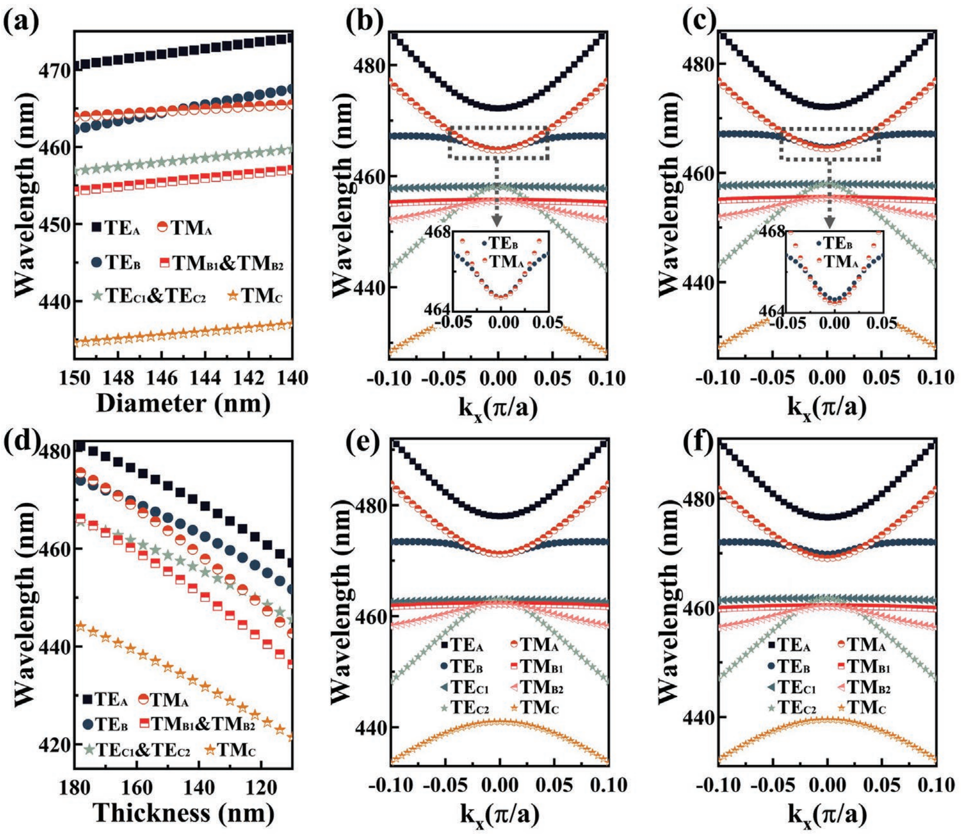

Figure 2. a) Eigen-wavelength changes of TE-like and TM- like modes with different diameter of nanoholes. The remained parameters of PhC slab are chosen to be $a = 270$ nm, $n_p = 2.02$, $n_s = n_b = 1.47$, and $t = 154$ nm, respectively. TE_A, TE_B, TE_{C1}&TE_{C2} modes are indicated by black squares, dark green circles, and light green stars. TM_A, TM_{B1}&TM_{B2}, and TM_C modes are denoted by half-filled wine circles, red squares, and orange stars. b,c) Band structures of photonic crystal slabs with $d = 145.5$ nm (b), and $d = 145$ nm (c). The other parameters are $a = 270$ nm, $n_p = 2.02$, $n_s = n_b = 1.47$ and $t = 154$ nm, respectively. The insets show the enlarged band structures of TE_B and TM_A around Γ point. d) Eigen-wavelength changes of TE-like and TM-like modes with different photonics crystal slab thickness. Other parameters of the PhC slab are chosen to be $a = 270$ nm, $n_p = 2.02$, $n_s = n_b = 1.47$, and $d = 140$ nm, respectively. TE_A, TE_B, TE_{C1}&TE_{C2} modes are indicated by black squares, dark green circles, and light green stars. TM_A, TM_{B1}&TM_{B2}, and TM_C modes are denoted by half-filled wine circles, red squares, and orange stars. e,f) Band structures of photonic crystal slabs with $t = 167$ nm (e), and $t = 162$ nm (f). The other parameters are $a = 270$ nm, $n_p = 2.02$, $n_s = n_b = 1.47$, and $d = 140$ nm, respectively. TE_A, TE_B, TE_{C1}, and TE_{C2} modes are represented by black squares, dark green circles, green triangles, and light green stars, while TM_A, TM_{B1}, TM_{B2}, and TM_C modes are represented by half-filled wine circles, red squares, pink triangles, and orange stars, respectively.

are marked by n_b, n_p, and n_s, respectively. To create an optically symmetric environment, the refractive indexes of background and substrate are set to the same ($n_b = n_s = 1.47$). We calculate the band structure of PhC slab with parameters being $a = 270$ nm, $d = 155$ nm, $h = 154$ nm, and $n_p = 2.02$. There are a series of TE-like and TM-like resonance modes, which are labeled as $TE_A/TE_B/TE_{C1}/TE_{C2}$ and $TM_A/TM_{B1}/TM_{B2}/TM_C$, as shown in Figure 1b. TE_A, TE_B, TE_{C1}, and TE_{C2} modes are represented by black squares, dark green circles, green triangles, and light green stars, while TM_A, TM_{B1}, TM_{B2}, and TM_C modes are represented by half-filled wine circles, red squares, pink triangles, and orange stars. Eigenstates of different photonic modes at Γ point are shown in Figure 1c. Among all these states, TE_{C1}, TE_{C2}, TM_{B1}, and TM_{B2} are double-degenerate eigenmodes, which possess radiation losses. The field distribution of TE_{C1} and TM_{B1} can be obtained from TE_{C2} and TM_{B2} through a $\pi/2$ rotation. The remained four resonant states (TE_A, TE_B, TM_A, and TM_C) are symmetry-protected BIC modes. Figure 1d,e presents the calculated Q-factors of TE- and TM-like modes, respectively. It is clearly shown that Q-factors of TE- and TM-like BICs are extremely high compared to double-degenerate leaky eigenmodes, meaning the dramatically suppressed radiation losses of BICs.

By tuning the geometric parameters of the PhC slab, the eigen-wavelengths of a pair of orthogonal BICs can coalesce with each other, giving rise to the merged BIC, which is called as the vector BIC. **Figure 2**a shows the evolution of these TE-like and TM-like modes at Γ point as a function of the diameter of nanoholes. Here, TE_A, TE_B, TE_{C1}&TE_{C2} modes are indicated by black squares, dark green circles, and light green stars. TM_A, TM_{B1}&TM_{B2}, and TM_C modes are denoted by half-filled wine circles, red squares, and orange stars. The remained parameters of PhC slab are chosen to be $a = 270$ nm, $n_p = 2.02$, $n_s = n_b = 1.47$ and $t = 154$ nm, respectively. We can see that the eigen-wavelengths of all modes are decreasing with the increase of the diameter of nanoholes. If the diameter is relatively large (d >145.5 nm), TE_B mode has a smaller eigen-wavelength compared to TM_A mode. However, with the decrease of the diameter, the eigen-wavelength for $\mathrm{TE_B}$ mode increases much faster than that of the $\mathrm{TM_A}$ mode, and, at a certain point, these two modes merge with each other, giving rise to a vector BIC. This formation of vector BIC can be demonstrated more clearly by calculating the evolution of band structures. As for the case with d = 155 nm, the eigen-wavelength of $\mathrm{TE_B}$ mode is much smaller than that of $\mathrm{TM_A}$ mode, and these two bands are far from each other, as shown in Figure 1b. When the diameter gets smaller, eigen-wavelengths of $\mathrm{TE_B}$ and $\mathrm{TM_A}$ get closer and become coincident at Γ point at d = 145.5 nm, as shown in Figure 2b. The bands of $\mathrm{TE_B}$ and $\mathrm{TM_A}$ modes are superposition with each other around Γ point, as seen in the inset of Figure 2b, indicating the formation of vector BIC. By further decreasing the diameter, the eigen-wavelength of $\mathrm{TE_B}$ will get larger than that $\mathrm{TM_A}$ of at Γ point, making these two bands have cross points around Γ point. The band structure of PhC with d = 145 nm is shown in Figure 2c, the two cross points of $\mathrm{TE_B}$ and $\mathrm{TM_A}$ around Γ point are shown in the inset of Figure 2c. These two cross points are vector quasi-BICs.

Besides of the diameter of array holes, vector BICs can also be design in the PhC slab by varying the thickness of the PhC slab. Figure 2d shows the evolution of eigen-wavelength for these TE- and TM-like modes at Γ point as a function of the thickness of PhC slabs. Other parameters are chosen to be a = 270 nm, n_p = 2.02, $n_\mathrm{s} = n_\mathrm{b}$ = 1.47, and d = 140 nm, respectively. There are three points where eigen-wavelengths of TE- and TM- like modes coalesced, that are $\mathrm{TE_B}$ and $\mathrm{TM_A}$ coalesced at h = 167 nm, $\mathrm{TE_{C1}}$/$\mathrm{TE_{C2}}$ and $\mathrm{TM_A}$ coalesced at h = 124 nm, and $\mathrm{TE_{C1}}$/$\mathrm{TE_{C2}}$ and $\mathrm{TM_{B1}}$/$\mathrm{TM_{B2}}$ coalesced at h = 172 nm. Among these points, only the first point (where $\mathrm{TE_B}$ and $\mathrm{TM_A}$ coalesced at h = 167 nm) is formed by two BIC states, corresponding to a vector BIC. The band structure of PhC slab with thickness being 167 nm is shown in Figure 2b. It is shown that bands of $\mathrm{TE_B}$ mode and $\mathrm{TM_A}$ mode are overlap with each other at Γ point, indicating the formation of a vector BIC. When the PhC thickness gets even smaller, the eigen-wavelength of $\mathrm{TE_B}$ mode is larger than that of $\mathrm{TM_A}$ mode, and these two bands can have cross points around Γ points, as shown in Figure 2c.

In addition, with the tuning of other parameters (such as the period of PhC slab), vector BICs can also be formed by merging other BIC modes (such as $\mathrm{TE_A}$, $\mathrm{TM_C}$, etc.). In the following, we mainly focus on the vector BIC formed by $\mathrm{TE_B}$ and $\mathrm{TM_A}$ modes to illustrate the exotic properties of vector BICs.

3. Giant Superchiral Fields Generated by Vector BICs

In this part, we show that vector BICs can produce strong and single-handed superchiral fields, which enable the ultrasensitive chirality detection. Early works proposed by Tang and Cohen[42,43] have shown that superchiral fields, which possess larger optical chirality than CPLs, can significantly enhance molecular chiroptical effects, allowing for ultrasensitive detection of chiral molecules. Motivated by this work, there are various works studying the creation of superchiral near fields by artificial structures. According to the definition of optical chirality $C = -\varepsilon_0 \omega Im(E * \cdot B)/2$, it is noted that there are two requirements for the generation of homogeneous superchiral fields. The first is that the enhanced E and B fields should have a large spatial overlap, and are parallel with each other. The second is that a $\pi/2$ phase shift between these two modes should exist. Due to the ultrahigh Q-factors of both TE-like and TM-like BICs, the electric and magnetic fields can be greatly enhanced around Γ point. Besides, the magnetic (electric) fields of $\mathrm{TE_B}$ mode is paralleled to the electric (magnetic) field of $\mathrm{TM_A}$ mode. In this consideration, our proposed vector BICs can generate extremely enhanced superchiral fields by exciting the PhC slab with CPLs.

To illustrate this effect, we calculate the enhancement of chiral field ($\mathrm{C/C_0}$) around the PhC slab with different diameters of holes. Here, $\mathrm{C_0}$ represents the chiral field of CPLs, and C represents the averaged chiral field around the PhC slab. **Figure 3**a shows the enhancement of chiral field under the normal excitation with d = 155 nm. We can see that the chiral field enhancement is near zero at $\mathrm{TE_B}$ or $\mathrm{TM_A}$ modes, as indicated by arrows in Figure 3a. This is consistent to the fact that BIC modes are dark states, that cannot be excited. In addition, there is a small enhancement of chiral fields around double-degenerated states of $\mathrm{TE_{C1}}$&$\mathrm{TE_{C2}}$ and $\mathrm{TM_{B1}}$&$\mathrm{TM_{B2}}$, which are closed to each other to create a quasi-fourfold degenerated state, as marked by arrow "A" in Figure 3a. The corresponding transmission spectrum is presented in Figure 3b, which is in a good agreement to the enhancement of chiral field and the band structure calculated above. For the oblique incidence with k = 0.0276 rad m^{-1}, which corresponds to an incident angle of 0.93°, all modes of $\mathrm{TE_{C1}}$&$\mathrm{TE_{C2}}$, $\mathrm{TM_{B1}}$&$\mathrm{TM_{B2}}$, $\mathrm{TE_B}$, $\mathrm{TM_A}$, and $\mathrm{TE_A}$ are excited. However, the quasi-BIC modes are apart from each other, making the enhancement of chiral near fields become small, as shown in Figure 3c.

Figure 3e shows the chiral field enhancement under normal excitation for PhC with d = 145.5 nm, which possesses vector BIC at Γ point. Because BIC modes are hard to excite, the chiral field enhancement is still near zero, as indicated by the arrow in Figure 3e,f shows the corresponding transmission spectrum. We can see that there are only two valleys corresponding to the two double-degenerate states ($\mathrm{TE_{C1}}$&$\mathrm{TE_{C2}}$, $\mathrm{TM_{B1}}$&$\mathrm{TM_{B2}}$), and BIC modes are not excited, being accordance with the enhancement of chiral fields. Figure 3g shows the enhancement of chiral field at k = 0.0276 rad m^{-1} and the corresponding transmission spectrum is plotted in Figure 3h. It is shown that modes of $\mathrm{TE_B}$ and $\mathrm{TM_A}$ are excited, but they are not coalesced with each other. Therefore, there is only mild chiral field enhancement around $\mathrm{TE_B}$ and $\mathrm{TM_A}$, as marked by the arrow in Figure 3g.

As seen from the above calculation, although the vector BIC has great potential to create giant chiral field enhancement, it is hard to be excited. Thus, we choose quasi-BIC states to achieve homogeneous superchiral fields. Figure 3i shows the chiral field enhancement under normal excitation for PhC with d = 145 nm. At Γ point, modes of $\mathrm{TE_B}$ and $\mathrm{TM_A}$ are apart from each other, and the chiral field enhancement is near zero at $\mathrm{TM_A}$ or $\mathrm{TE_B}$ modes. The transmission spectrum in Figure 3j is consistent with the chiral field enhancement. As for k = 0.0276 rad m^{-1}, Q-factors for $\mathrm{TE_B}$ and $\mathrm{TM_A}$ modes are still very large. Thus, the electric and magnetic near fields for these two modes are also greatly enhanced. In addition, as seen from the transmission spectrum in Figure 3l, these two modes are effectively excited and are totally

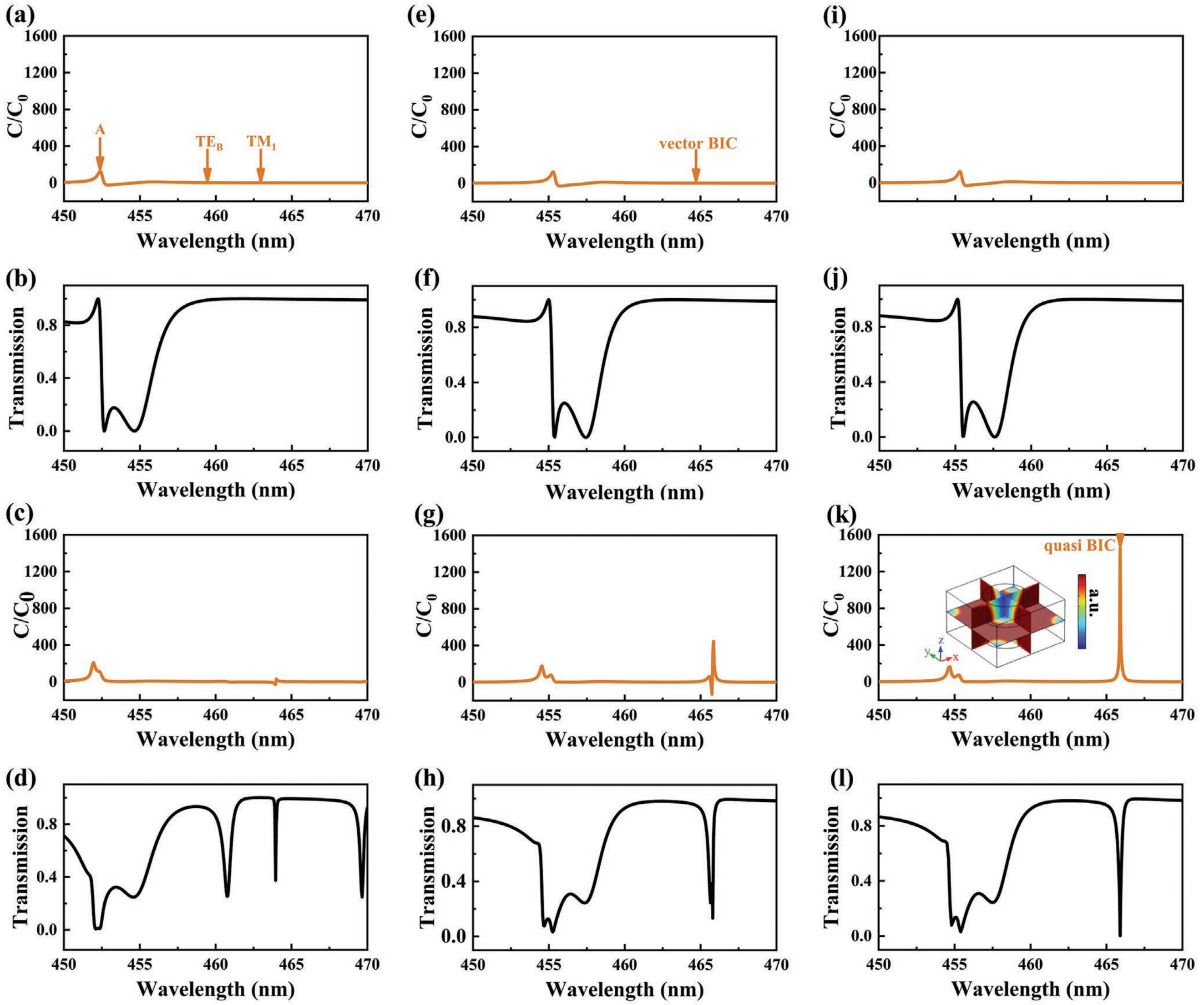

Figure 3. a) Chiral field enhancement for Si_3N_4 PhC under normal excitation with parameters of $a = 270$ nm, $h = 154$ nm, $n_b = n_s = 1.47$, and $d = 155$ nm. b) Transmission spectra of Si_3N_4 PhC under normal excitation with parameters of $a = 270$ nm, $h = 154$ nm, $n_b = n_s = 1.47$, and $d = 155$ nm. c) Chiral field enhancement for Si_3N_4 photonic crystal slabs with parameters of $a = 270$ nm, $h = 154$ nm, $n_b = n_s = 1.47$, and $d = 155$ nm at $k = 0.0276$ rad m^{-1}, corresponding to an incident angle of 0.93°. d) Transmission spectra of Si_3N_4 photonic crystal slabs with parameters of $a = 270$ nm, $h = 154$ nm, $n_b = n_s = 1.47$, and $d = 155$ nm at $k = 0.0276$ rad m^{-1}, corresponding to an incident angle of 0.93°. e) Chiral field enhancement for Si_3N_4 PhC under normal excitation with parameters of $a = 270$ nm, $h = 154$ nm, $n_b = n_s = 1.47$, and $d = 145.5$ nm. f) Transmission spectra of Si_3N_4 PhC under normal excitation with parameters of $a = 270$ nm, $h = 154$ nm, $n_b = n_s = 1.47$, and $d = 145.5$ nm. g) Chiral field enhancement for Si_3N_4 photonic crystal slabs with parameters of $a = 270$ nm, $h = 154$ nm, $n_b = n_s = 1.47$, and $d = 145.5$ nm at $k = 0.0276$ rad m^{-1}. h) Transmission spectra of Si_3N_4 photonic crystal slabs with parameters of $a = 270$ nm, $h = 154$ nm, $n_b = n_s = 1.47$, and $d = 145.5$ nm at $k = 0.0276$ rad m^{-1}. i) Chiral field enhancement for Si_3N_4 PhC under normal excitation with parameters of $a = 270$ nm, $h = 154$ nm, $n_b = n_s = 1.47$, and $d = 145$ nm. j) Transmission spectra of Si_3N_4 PhC under normal excitation with parameters of $a = 270$ nm, $h = 154$ nm, $n_b = n_s = 1.47$, and $d = 145$ nm. k) Chiral field enhancement for Si_3N_4 photonic crystal slabs with parameters of $a = 270$ nm, $h = 154$ nm, $n_b = n_s = 1.47$, and $d = 145$ nm at $k = 0.0276$ rad m^{-1}. l) Transmission spectra of Si_3N_4 photonic crystal slabs with parameters of $a = 270$ nm, $h = 154$ nm, $n_b = n_s = 1.47$, and $d = 145$ nm at $k = 0.0276$ rad m^{-1}.

coalesced. Hence, the conditions of the chiral field enhancement are fulfilled. As seen in Figure 3k, this quasi-vector BIC generates a three orders of magnitude amplification of chiral fields, which has never been achieved in previous studies. Besides, the chiral field is homogeneous all over the PhC, as seen in the inset of Figure 3k. In addition, because of the larger Q-factor, this field enhancement could be more enormous with proper design to make the cross points of TE_B and TM_A closer to Γ point.

4. Experimental Observation of Vector BICs

In this section, we illustrate the observation of vector BICs in experimental. First, many Si_3N_4 photonic crystal slabs with different sizes of nanoholes are fabricated on the silica substrate, where the structural parameters are consistent to that used in simulations. A layer of Si_3N_4 with the thickness of 154 nm is deposited on the silica substrate. Then, a series of cylindrical hole

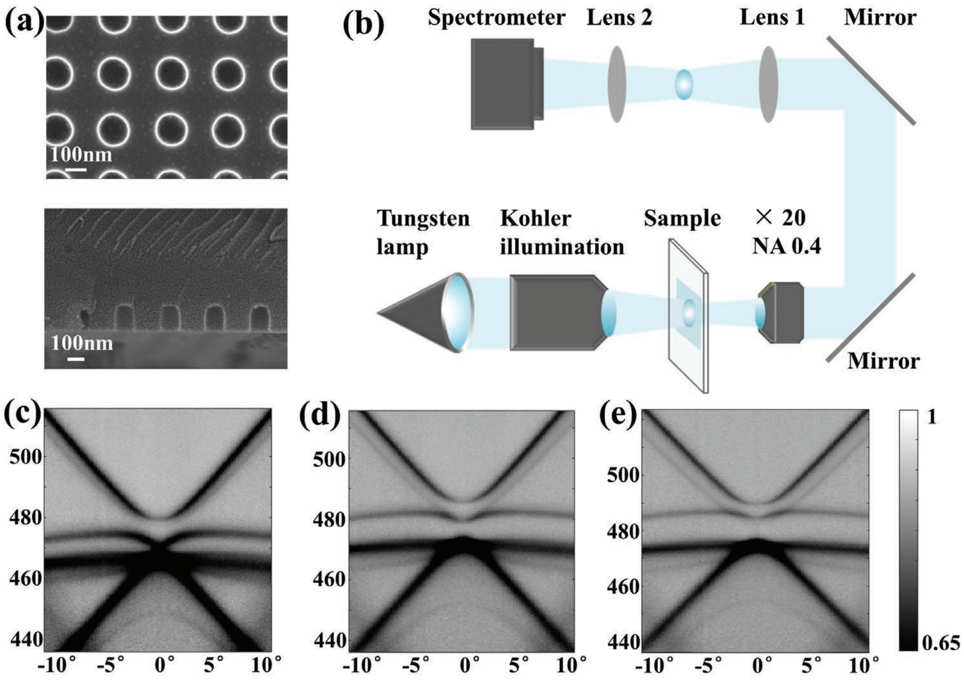

Figure 4. a) Top and side views of the scanning electron microscope images for the fabricated sample. b) Experimental setups for the measurement of band structures. c–e) Measured band structures of Si_3N_4 cylinder arrays with $a = 270$ nm, $h = 154$ nm, $d = 150$ nm (c), $d = 130$ nm (d), and $d = 120$ nm (e).

square arrays are fabricated in Si_3N_4 layer by combining e-beam lithography and reactive ion etching. The size of each hole array is about 450 × 450 μm^2. The diameters of cylinder holes in different arrays are changing from 130 to 170 nm, where both the period (a = 270 nm) and the height (h = 154 nm) are fixed. To create an optically symmetric environment, we etch the holes through the entire Si_3N_4 layer and immerse the sample in an optical liquid that is index-matched to silica. Scanning electron microscope (SEM) images of the sample are shown in **Figure 4**a.

To experimentally demonstrate the formation of vector BICs, we measure the angle-resolved transmission spectra for Si_3N_4 PhCs with different diameters of nanoholes. These spectra are measured by using the homemade polarization-resolved momentum-space imaging spectroscopy based on Fourier analysis,[44] as illustrated in Figure 4b. The working principle is that the information carried by the back focal plane of an objective lens is consistent with the momentum-space (Fourier-space) information of the radiation field from the sample. Figure 4c shows the measured band structure for PhC with d = 150 nm. The darkness of the spectrum represents the transmittivity of each mode. The darker line represents a higher transmission. It is clearly shown that this band structure is totally in agreement with the simulation result. There are series of TE-like and TM-like resonance modes. We note that frequency bands described by darker (lighter) lines represent TE-like (TM-like) modes. This is because that the Q-factor of TM-like mode is larger than that of TE-like mode, making TM-like mode much hard be excited. Additionally, the band line is much lighter at Γ point for TE_A, TE_B, TM_A, and TM_C modes, indicating the suppressed radiation loss at Γ point. However, different from perfect BICs in simulations, we can see that the transmittivities at Γ point for TE_A, TE_B, TM_A, and TM_C modes are not zero. This results from the breaking of C_4 rotation symmetry by elliptical holes in the fabricated sample. It is noted that the eigen-wavelength of TE_B mode is much larger than TM_A, and these two bands are far from each other.

When the diameter of nanoholes gets smaller, bands of TE_B and TM_A get closer and become overlapped with each other around Γ point at d = 130 nm, as shown in Figure 4d, indicating the formation of vector quasi-BIC. By further decreasing the diameter, the eigen-wavelength of TE_B will get larger than that of TM_A at Γ point, making these two bands have cross points around Γ point. The measured band structure of PhC with d = 120 nm is shown in Figure 4e. Eigen-wavelength of TE_B at Γ point will be even larger when the diameter gets smaller further, and the cross points will be more far away from Γ point. With all the above measurement, we find that the band structure of PhC slabs can be effectively tuned by changing diameters of cylinder holes, and the vector quasi-BIC is experimentally observed with merging modes of TE_B and TM_A. All experiment results are in good agreement with numerical results. The little deviation between experiment and simulation is due to the tiny difference of back refractive index used in experiment and simulation.

5. Conclusion

In conclusion, we have theoretically designed and experimentally observed the vector BICs in PhC slabs. In theory, we constructed symmetry-protected vector BICs by suitably tuning geometric parameters of the PhC slab. The formation of vector BICs is demonstrated by the by the coalesce of eigen-wavelengths of a pair of TE-like and TM-like BIC modes. Homogeneous near chiral field which is three orders of magnitude larger than CPLs can be achieved by exciting the PhC slab with the vector BIC. In experiment, we fabricated Si_3N_4 PhC slabs with different diameters of nanoholes and measured their associated band structures. The measured band structures are totally consistent with simulations, manifesting the realization of vector BICs. With strong and homogenous superchiral fields, our designed PhC slabs could become an ideal platform to perform surface-enhanced fluorescence CD and Raman optical activity of chiral molecules.

6. Experimental Section

Sample Fabrication: A layer of Si3N4 film with thickness of 154 nm was grown with the plasma enhanced chemical vapor deposition (PECVD) method on a 500-µm-thick silica substrate. A layer of 300-nm polymethyl methacrylate (PMMA) was spun-coated on the Si3N4 film as e-beam photoresist. After exposure and development, resist patterns were formed. Then these patterns were transferred to Si3N4 with an anisotropic plasma mixture of CF4/CHF3/O2 gas, using PMMA as an etching mask.

Spectra Measurement: The transmission spectra were measured using a home-made polarization-resolved momentum-space imaging spectroscopy built based on an Olympus micro-scope. The source is a tungsten lamp and the incident light is focused on to sample by an objective (20_magnitude, NA 0.4). The transmission light from the sample was imaged onto the entrance slit of imaging spectrometer (Princeton Instruments IsoPlane-320) through a series of convex lens.

Acknowledgements

H.Z., W.Z., and S.C. contributed equally to this work. This work was supported by National Science Foundation of China (Nos. 11904021, 12234007, 12221004), and China National Key Basic Research Program under Grant No. 2022YFA1404800.

Conflict of Interest

The authors declare no conflict of interest.

Data Availability Statement

The data that support the findings of this study are available from the corresponding author upon reasonable request.

Keywords

bound states in the continuum, photonic crystal slabs, superchiral fields

Received: December 27, 2022
Revised: February 9, 2023

---

[1] J. Von Neumann, E. Wigner, *Phys. Z.* **1929**, *30*, 465.
[2] C. W. Hsu, B. Zhen, J. Lee, S.-L. Chua, S. G. Johnson, J. D. Joannopoulos, M. Soljačić, *Nature* **2013**, *499*, 188.
[3] B. Zhen, C. W. Hsu, L. Lu, A. D. Stone, M. Soljačić, *Phys. Rev. Lett.* **2014**, *113*, 257401.
[4] A. Kodigala, T. Lepetit, Q. Gu, B. Bahari, Y. Fainman, B. Kanté, *Nature* **2017**, *541*, 196.
[5] S. T. Ha, Y. H. Fu, N. K. Emani, Z. Pan, R. M. Bakker, R. Paniagua-Domínguez, A. I. Kuznetsov, *Nat. Nanotechnol.* **2018**, *13*, 1042.
[6] Y.-X. Xiao, G. Ma, Z.-Q. Zhang, C. T. Chan, *Phys. Rev. Lett.* **2017**, *118*, 166803.
[7] H. M. Doeleman, F. Monticone, W. den Hollander, A. Alù, A. F. Koenderink, *Nat. Photonics* **2018**, *12*, 397.
[8] E. N. Bulgakov, D. N. Maksimov, *Phys. Rev. Lett.* **2017**, *118*, 267401.
[9] B. Wang, W. Liu, M. Zhao, J. Wang, Y. Zhang, A. Chen, F. Guan, X. Liu, L. Shi, J. Zi, *Nat. Photonics* **2020**, *14*, 623.
[10] C. Huang, C. Zhang, S. Xiao, Y. Wang, Y. Fan, Y. Liu, N. Zhang, G. Qu, H. Ji, J. Han, *Science* **2020**, *367*, 1018.
[11] J. Jin, X. Yin, L. Ni, M. Soljačić, B. Zhen, C. Peng, *Nature* **2019**, *574*, 501.
[12] X. Yin, J. Jin, M. Soljačić, C. Peng, B. Zhen, *Nature* **2020**, *580*, 467.
[13] Q. Song, J. Hu, S. Dai, C. Zheng, D. Han, J. Zi, Z. Zhang, C. T. Chan, *Sci. Adv.* **2020**, *6*, eabc1160.
[14] B.-J. Yang, M. Saeed Bahramy, N. Nagaosa, *Nat. Commun.* **2013**, *4*, 1524.
[15] V. A. Sablikov, A. A. Sukhanov, *Phys. Lett. A* **2015**, *379*, 1775.
[16] K. Ding, G. Ma, M. Xiao, Z. Zhang, C. T. Chan, *Phy. Rev. X* **2016**, *6*, 021007.
[17] K. Hirose, Y. Liang, Y. Kurosaka, A. Watanabe, T. Sugiyama, S. Noda, *Nat. Photonics* **2014**, *8*, 406.
[18] S. Romano, G. Zito, S. N. L. Yépez, S. Cabrini, E. Penzo, G. Coppola, I. Rendina, V. Mocellaark, *Opt. Express* **2019**, *27*, 18776.
[19] Y. Liu, W. Zhou, Y. Sun, *Sensors* **2017**, *17*, 1861.
[20] H. Barkaoui, K. Du, Y. Chen, S. Xiao, Q. Song, *Phys. Rev. B* **2023**, *107*, 045305.
[21] J. Li, J. Ren, X. Zhang, *J. Opt. Soc. Am. B* **2017**, *34*, 559.
[22] B. K. Thomson, W. Thomson, *Baltimore Lectures on Molecular Dynamics and the Wave Theory of Light*, Cambridge University Press, Cambridge, UK **2010**.
[23] L. A. Nguyen, H. He, C. Pham-Huy, *Int. J. Biomed. Sci.* **2006**, *2*, 85.
[24] S. Mitra, P. Chopra, *Indian J. Anaesth.* **2011**, *55*, 556.
[25] V. K. Valev, J. J. Baumberg, C. Sibilia, T. Verbiest, *Adv. Mater.* **2013**, *25*, 2517.
[26] C. King, F. Kendrick, *Lancet* **1962**, *280*, 1116.
[27] S. Yoo, Q.-H. Park, *Nanophotonics* **2019**, *8*, 249.
[28] J. T. Collins, C. Kuppe, D. C. Hooper, C. Sibilia, M. Centini, V. K. Valev, *Adv. Opt. Mater.* **2017**, *5*, 1700182.
[29] Y. Luo, C. Chi, M. Jiang, R. Li, S. Zu, Y. Li, Z. Fang, *Adv. Opt. Mater.* **2017**, *5*, 1700040.
[30] V. E. Bochenkov, T. I. Shabatina, *Biosensors* **2018**, *8*, 120.
[31] J. Mejía-Salazar, O. N. Oliveira, *Chem. Rev.* **2018**, *118*, 10617.
[32] E. Hendry, T. Carpy, J. Johnston, M. Popland, R. Mikhaylovskiy, A. Lapthorn, S. Kelly, L. Barron, N. Gadegaard, M. Kadodwala, *Nat. Nanotechnol.* **2010**, *5*, 783.
[33] M. Schäferling, D. Dregely, M. Hentschel, H. Giessen, *Phys. Rev. X* **2012**, *2*, 031010.
[34] M. Schäferling, X. Yin, H. Giessen, *Opt. Express* **2012**, *20*, 26326.
[35] T. Davis, E. Hendry, *Phys. Rev. B* **2013**, *87*, 085405.
[36] A. Vázquez-Guardado, D. Chanda, *Phys. Rev. Lett.* **2018**, *120*, 137601.
[37] F. Graf, J. Feis, X. Garcia-Santiago, M. Wegener, C. Rockstuhl, I. Fernandez-Corbaton, *ACS Photonics* **2019**, *6*, 482.
[38] R. Tullius, A. S. Karimullah, M. Rodier, B. Fitzpatrick, N. Gadegaard, L. D. Barron, V. M. Rotello, G. Cooke, A. Lapthorn, M. Kadodwala, *J. Am. Chem. Soc.* **2015**, *137*, 8380.
[39] R. Wang, P. Wang, Y. Liu, W. Zhao, D. Zhai, X. Hong, Y. Ji, X. Wu, F. Wang, X. Zhang, *J. Phys. Chem. C* **2014**, *118*, 9690.
[40] T. Wu, J. Ren, R. Wang, X. Zhang, *J. Phys. Chem. C* **2014**, *118*, 20529.
[41] W. Zhang, T. Wu, R. Wang, X. Zhang, *J. Phys. Chem. C* **2017**, *121*, 666.
[42] Y. Tang, A. E. Cohen, *Phys. Rev. Lett.* **2010**, *104*, 163901.
[43] Y. Tang, A. E. Cohen, *Science* **2011**, *332*, 333.
[44] Y. Zhang, A. Chen, W. Liu, C. W. Hsu, B. Wang, F. Guan, X. Liu, L. Shi, L. Lu, J. Zi, *Phys. Rev. Lett.* **2018**, *120*, 186103.